*J. Fluid Mech.* (1981), *vol.* 102, *pp.* 405–430
*Printed in Great Britain*



# Analytical and numerical aspects of the electromagnetic stirring induced by alternating magnetic fields

By Y. R. FAUTRELLE
Institut de Mécanique de Grenoble, B.P. 53 Centre de Tri, 38041 Grenoble Cedex

(Received 13 October 1978 and in revised form 24 July 1980)

The dynamic effects of an alternating magnetic field on containers of conducting fluid are investigated in two special cases: (i) an infinitely long circular cylinder in a uniform magnetic field normal to the generators; (ii) a truncated circular cylinder in a uniform magnetic field parallel to the axis. Neglecting the motion effects in Maxwell's equations, the problem is conveniently decoupled into electromagnetic and dynamic parts. Using either analytical or numerical solutions of the electromagnetic equations, the electromagnetic forces are calculated and introduced in the motion equations. In the first case, asymptotic solutions of the Navier–Stokes equations valid for high frequencies are calculated and compared with numerical solutions obtained for the same geometry. The second case has been studied numerically, and the solutions are presented and interpreted.

## 1. Introduction

There have been many recent developments in the field of electromagnetic stirring by alternating magnetic fields in liquid metal furnaces or crucibles. The main reason is that in most metallurgical devices using induction processes electric currents are set up in the bath, and it is necessary to cope with electromagnetic forces and their effects on the liquid metal. Knowledge of these forces is a necessary first step for the conception and optimization of such devices. Obviously, rotating or travelling magnetic field systems provide more efficient stirring than do alternating current systems. However, it is well-known by engineers that alternating field systems provide the most efficient designs for heating and melting. Therefore, the question is: how can we control the stirring in such systems? Note that stirring may have both useful and adverse effects. On the one hand, it is a means of improving the homogeneity of the bath, but on the other hand, stirring may lead to a rapid erosion of the refractory walls.

So far, mainly numerical approaches have been undertaken in order to solve this problem.† We mention here the works of Szekely & Nakanishi (1975), and Tarapore & Evans (1976) who considered a crucible in a coil and computed the motions taking account of turbulence. The computations were performed for special cases of metallurgical and practical interest. They noticed that the motion is organized in cellular patterns whose size depends on the location of the induction coil. However, no explanation of that phenomenon has been given. Few analytical works have been

† The reader is referred to Moreau's survey (1980) for further details.

0022-1120/81/4713-2910 $02.00 

carried out. Sneyd (1971) treated the two-dimensional case of a cylinder in a uniform alternating magnetic field (case I below). However, he only considered very weak field strengths the resulting motion being dominated by viscosity. Sneyd (1979) also gave a method of calculating the electromagnetic force distribution in a closed container in the limit of high frequencies. Tir (1975) attempted a global approach by calculating energy budgets in order to determine the efficiency of the stirring.

The above studies were carried out for special configurations, and there exists as yet little attempt to explain the detailed mechanism of electromagnetic stirring by A.C. fields. A deeper understanding of the action of the Lorentz forces on the motion is still required. It is of particular interest to determine the precise role of some basic parameters such as the frequency $f$, the strength of the magnetic field $B_0$ (or the induction currents) and the viscosity $\nu$ on the cellular-type flow configuration and on the order of magnitude of the velocities. Therefore, using both analytical and numerical tools, we have studied two special configurations:

*Case I.* An infinite circular cylinder in a uniform transverse magnetic field.

*Case II.* A truncated circular cylinder in a uniform axial magnetic field.

In this study, some non-dimensional numbers will be employed to represent the above basic parameters. First, the frequency will be characterized by the magnetic Reynolds number $R_\omega$ based upon the frequency as follows:

$$R_\omega = \mu\sigma\omega L^2, \tag{1.1}$$

where $\mu$ is the magnetic permeability of the medium, $\sigma$ the electrical conductivity, $L$ a typical length scale of the crucible and $\omega$ the pulsation defined by

$$\omega = 2\pi f. \tag{1.2}$$

The importance of the electromagnetic forces with respect to the viscosity is given by an interaction parameter $R$ defined by

$$R = u_0 L/\nu, \tag{1.3}$$

where $u_0$ is the Alfvén velocity based on the applied field strength,

$$u_0 = B_0/(\mu\rho_0)^{\frac{1}{2}}, \tag{1.4}$$

where $\rho_0$ is the density of the fluid. The containers will be assumed to be closed, i.e. without free surface. In the analytical study it will be assumed that

$$R_\omega \gg 1 \tag{1.5}$$

(but displacement current will be neglected throughout). The actual magnetic Reynolds number $R_m$ based upon the velocity, namely

$$R_m = \mu\sigma u L, \tag{1.6}$$

where $u$ is a typical velocity scale of the motion, will be assumed to be much smaller than $R_\omega$. Hence the electric currents induced by the motion of the fluid particles across the lines of forces, i.e. $\sigma\mathbf{u}\times\mathbf{B}$ will be negligible compared with the electric currents induced by the pulsation of the applied magnetic field. This assumption allows us to consider separately the electromagnetic problem and the dynamic one as in the related rotating field problem, Moffatt (1965). As for the motion, the flow will be assumed to be laminar. In practical situations, the motion is likely to be

turbulent. Nevertheless, we suppose that the analysis may be applied to the well-organized large scale structures of the flow, the viscosity being then interpreted as an eddy viscosity. Temperature effects and consequently buoyancy forces will be neglected. This is justified in appendix B, where estimates are made of the order of magnitude of temperature gradients, and buoyancy forces are compared to the Lorentz forces in a standard practical situation. Moreover, owing to the large value of the frequency of the applied field, the inertial response of the fluid to the periodic part of the Lorentz force will be neglected (see Moreau 1980).

In § 2, the general equations of the problem are set up. Special forms of both Maxwell and Navier–Stokes equations are derived within the high-frequency limit. The case of the infinite circular cylinder is investigated in § 3. An asymptotic theory valid for $R_\omega \gg 1$ is compared with numerical calculations carried out in the same geometry for various values of $R_\omega$. In § 4 we give some numerical solutions of the Navier–Stokes equations in the case of a truncated circular cylinder. Finally, in § 5 some concluding remarks are made about the role and the importance of turbulence.

## 2. The general equations

### 2.1. *The electromagnetic aspects*

In this section we shall first give the general form of the Maxwell equations and the expression for the electromagnetic forces. Then their special form in the high frequency limit will be derived. Most of the results given below are well known and have been established in detail by Khaletzky (1976) and Sneyd (1971, 1979). However, to make the paper self-constrained, the main results will be recalled briefly. Attention will be focused especially on cases I and II.

(*a*) *The general case.* Under the assumption $R_m \ll R_\omega$ (§ 1), the electromagnetic and dynamic problems are decoupled. The first step is therefore to find the distribution of the magnetic field $\mathbf{B}$, the electric currents $\mathbf{j}$ induced throughout the body of conducting fluid $\mathscr{D}$ by an external alternating magnetic field and to calculate the $\mathbf{j} \times \mathbf{B}$ force.

The magnetic field distribution is governed by the Maxwell's equations. Assuming that the problem is either two-dimensional (case I) or axisymmetric (case II), these reduce to a single equation governing the one-component vector potential $A'\mathbf{i}_3$, namely

$$\nabla \times (\nabla \times A'\mathbf{i}_3) = -\mu\sigma \frac{\partial A'}{\partial t}\mathbf{i}_3, \tag{2.1}$$

where $\mathbf{i}_3$ has to be identified either with $\mathbf{i}_z$ in the two-dimensional case in cylindrical co-ordinates $(r, \theta, z)$ ($z$ being the axis of the cylinder) or with $\mathbf{i}_\theta$ in an axisymmetric geometry $(z, r, \theta)$, $z$ being the symmetry axis. If the applied magnetic field is a sinusoïdal function of time, then $A'$ can be sought in the form

$$A' = \mathscr{R}\{\hat{A}e^{i\omega t}\} \quad \text{with} \quad \hat{A} = |A|e^{i\phi}. \tag{2.2}$$

The vector potential is described by its phase $\phi$ and its amplitude $|A|$ which are both functions of the co-ordinates. The magnetic field $\mathbf{B}$ is given by

$$\mathbf{B} = \nabla \times (A'\mathbf{i}_3). \tag{2.3}$$

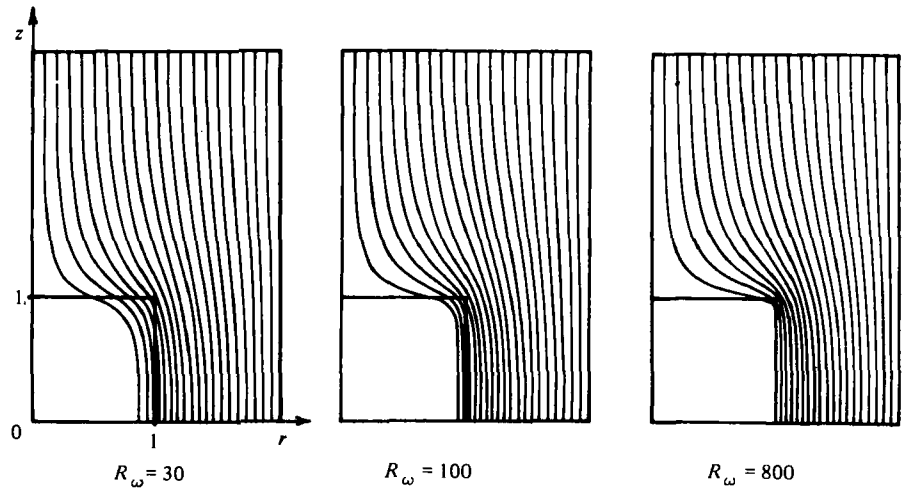


FIGURE 1. Numerical solutions of Maxwell equations. The geometry consists of a truncated circular cylinder in a uniform magnetic field (case II). The computed magnetic lines of forces are drawn for various values of $R_\omega$ in a half-meridian plane.

As for the boundary conditions, the magnetic field must be continuous across the boundary. Thus, from (2.3) we require the derivative of $A'$ to be continuous across the boundary of $\mathscr{D}$. The medium outside $\mathscr{D}$ will be assumed to be insulating as well as the wall of the crucible. The magnetic field is assumed to be uniform at infinity, and so $A'$ behaves as follows:

$$\left.\begin{aligned} &A' \sim r\sin\theta \text{ in the two-dimensional geometry,} \\ &A' \sim r \text{ in the axisymmetric geometry.} \end{aligned}\right\} \tag{2.4}$$

Within the crucible the electric currents are calculated from Ohm's law in the form

$$\mathbf{j} = -\sigma\frac{\partial A'}{\partial t}\mathbf{i}_3. \tag{2.5}$$

Thus, the electromagnetic forces may be obtained by using (2.2), (2.3), (2.5), namely

$$\mathbf{j}\times\mathbf{B} = (\sigma\omega|A|\sin(\omega t+\phi)\,\mathbf{i}_3)\times\nabla\times(|A|\cos(\omega t+\phi)\,\mathbf{i}_3). \tag{2.6}$$

Actually, under our assumptions (cf. § 1) we are only interested in the mean value of the Lorentz forces over a period (Moreau 1980). Hence, the driving forces are defined by

$$\langle\mathbf{j}\times\mathbf{B}\rangle \equiv \frac{1}{T}\int_0^T \mathbf{j}\times\mathbf{B}d\tau = -\frac{\sigma\omega}{2}|A|^2\nabla\phi, \tag{2.7}$$

where $T = 2\pi/\omega$. It is noteworthy that the curl of $\langle\mathbf{j}\times\mathbf{B}\rangle$ (cf. (2.7)), which is responsible for the motion, vanishes when the amplitude $|A|$ is constant. This occurs for example in an axisymmetric geometry for an infinitely long circular cylinder in a uniform magnetic field parallel to the axis. In this case, magnetic flux variations are responsible for any motion in accordance with Lenz's laws. (A similar result holds in the rotating field problem – see Moffatt 1980.)

In case I, the analytical solution has been obtained by Sneyd (1971). As for case II,

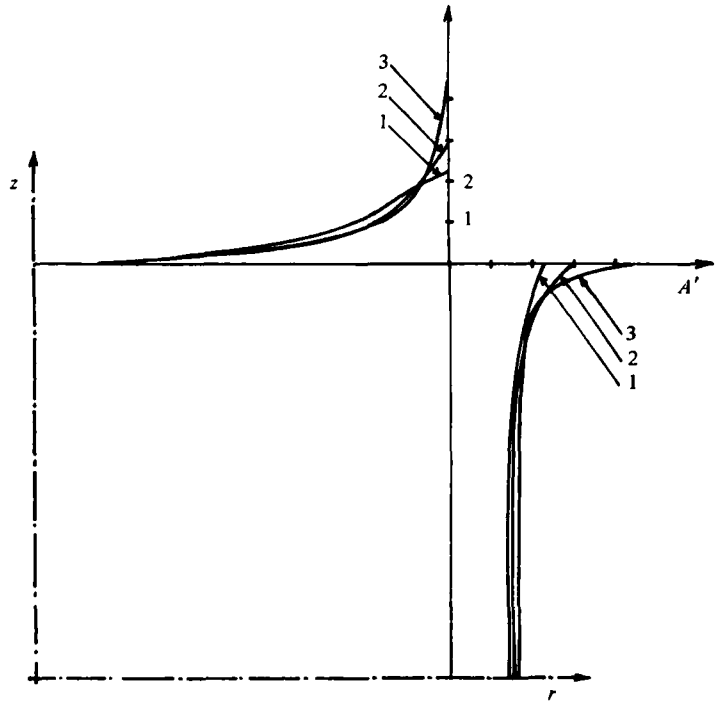


FIGURE 2. The computed value of the vector potential at the boundary is plotted along the wall for various values of $R_\omega$; $A'$ is normalized by $B_0\delta$. 1, $R_\omega = 30$; 2, $R_\omega = 100$; 3, $R_\omega = 800$.

equation (2.1) with the boundary condition (2.4) has been solved numerically, using a finite-difference scheme. The magnetic lines of force are shown in figure 1 for various values of $R_\omega$ (i.e. various frequencies) in a half meridian plane. We also give in figure 2 the distribution of the non-dimensional vector potential along the wall (the vector potential scale is $B_0\delta$, $\delta$ being the skin depth defined in (2.8) below).

(*b*) *The asymptotic case.* Inside $\mathscr{D}$ we may define a length scale $\delta$ corresponding to the thickness of the electromagnetic layer, namely

$$\delta = (\mu\sigma\omega/2)^{-\frac{1}{2}}. \tag{2.8}$$

In the high frequency limit, i.e.

$$\epsilon \equiv \delta/L = (2/R_\omega)^{\frac{1}{2}} \ll 1, \tag{2.9}$$

it is possible to calculate explicitly the vector potential. Formally, $\hat{A}$ may be expanded in power series of $\epsilon$, as follows:

$$\hat{A} = \hat{A}^{(0)} + \epsilon\hat{A}^{(1)} + \ldots. \tag{2.10}$$

Moreover, using Sneyd's procedure (1979), it is convenient to express (2.1) in a curvilinear frame with the boundary of $\mathscr{D}$ taken as a geodesic line. Let $x$ and $y$ be a system of curvilinear co-ordinates respectively along the boundary of $\mathscr{D}$ and normal to $\mathscr{D}$ (cf. figure 3 and appendix A where the definition of the local frame as well as the expression of the operator $\nabla\times\nabla\times(\,)$ are given). In terms of the dimensionless variables

$$x_* = x/L, \quad y_* = y/\delta, \quad \mathbf{B}_* = \mathbf{B}/B_0, \quad \hat{A}_* = \hat{A}/B_0\delta, \tag{2.11}$$

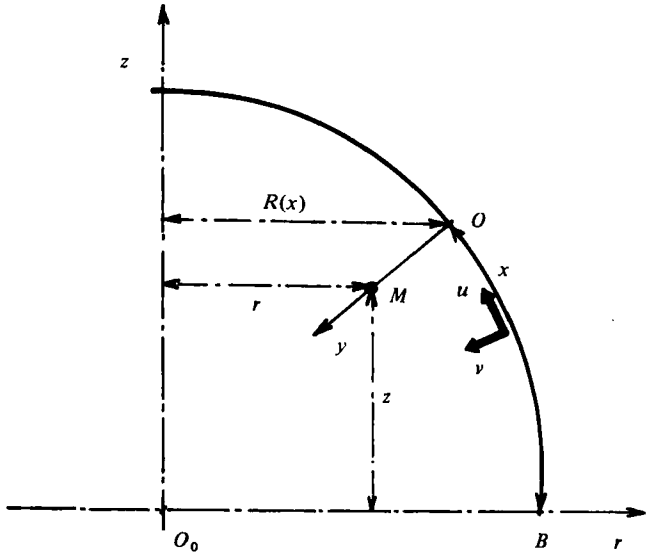


FIGURE 3. Sketch of the local frame defined from the boundary.

at the lowest-order equation (2.1) reduces to

$$\partial^2 \hat{A}^{(0)}/\partial y^2 = 2i\hat{A}^{(0)}, \tag{2.12}$$

where the asterisks have been dropped for convenience. Integrating (2.12) with the boundary condition

$$\hat{A}^{(0)} \to 0 \quad \text{as} \quad y \to +\infty,$$

and taking the real part yields the classical ('skin-effect') solution

$$A'^{(0)} = A^{(0)}(x)\, e^{-y} \cos(\omega t - y + \phi_0(x)). \tag{2.13}$$

$A^{(0)}(x)$, $\phi_0(x)$ respectively represent the vector potential and the phase along the boundary of $\mathscr{D}$. Outside $\mathscr{D}$ the magnetic field may be calculated by using the analogy between the magnetic field lines and the streamlines of the irrotational flow of an inviscid fluid past $\mathscr{D}$ (Moffatt 1978). Continuity of the magnetic field across the boundary of $\mathscr{D}$ then determines $A^{(0)}(x)$ and $\phi_0(x)$.

Consider for example case I. Using the above analogy outside $\mathscr{D}$ the dimensionless magnetic field component along the boundary, i.e. $B_\theta$ is

$$B_\theta = -2 \sin\theta \cos\omega t. \tag{2.14}$$

Continuity of the magnetic field yields

$$B_\theta = (\partial A'^{(0)}/\partial y)_{y=0}. \tag{2.15}$$

Thus, from (2.13) and (2.14), (2.15) serves to determine the functions $A^{(0)}$, $\phi_0$, namely

$$A^{(0)} = 2^{\frac{1}{2}} \sin\theta, \quad \phi_0 = -\pi/4. \tag{2.16}$$

In case II, there are two major difficulties in seeking analytic solutions. First (by analogy with potential flow theory), the magnetic field becomes infinite near the corner of the cylinder (when $R_\omega \to \infty$). This result is confirmed numerically below.

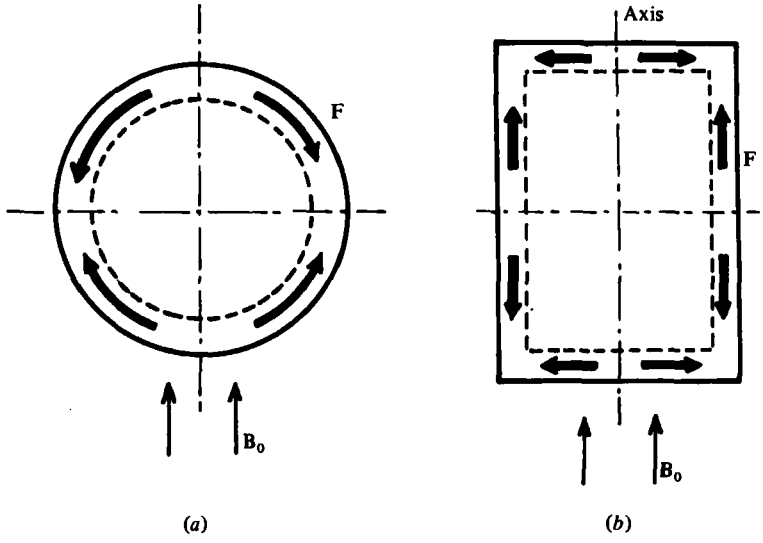


FIGURE 4. Sketch of the distribution of the rotational part of the electromagnetic forces, (*a*) case I, (*b*) case II.

Figure 2 shows that the vector potential distribution along the wall reaches a maximum value in the corner region and that maximum increases as $R_\omega$ increases. Secondly, it must be observed that equation (2.12) is no longer valid near the corner region since the curvature of the boundary becomes infinite. Consequently, the $x$ derivatives are no longer negligible with respect to the $y$ derivatives (cf. condition (A 8) of appendix A). This is illustrated in figure 1 where, for large $R_\omega$, the magnetic field lines cross the domain in the corner region.

In the high frequency limit the expression for the electromagnetic forces is simplified. Combining (2.7) and (2.13), the Lorentz forces take the following particular form in dimensional variables

$$\langle \mathbf{j} \times \mathbf{B} \rangle = \tfrac{1}{2}\sigma\omega\delta^{-1}|A|^2\mathbf{i}_y, \tag{2.17}$$

where

$$|A| = A^{(0)}(x)e^{-y/\delta}.$$

An equivalent formula was obtained by Sneyd (1979). Let us decompose the Lorentz forces into a gradient part $\nabla\Phi$ and a rotational part $\mathbf{F}$ as follows

$$\langle \mathbf{j} \times \mathbf{B} \rangle = \nabla\Phi + \mathbf{F}. \tag{2.18}$$

The potential $\Phi$ and $\mathbf{F}$ may be calculated explicitly from (2.17), (2.18), namely

$$\Phi = -\frac{\sigma\omega}{4}A^{(0)2}(x)\,e^{-2y/\delta}, \quad \mathbf{F} = \frac{\sigma\omega}{2}A^{(0)}\frac{dA^{(0)}}{dx}e^{-2y/\delta}\,\mathbf{i}_x. \tag{2.19}$$

In the non-dimensional variables (2.11) the expression for $\mathbf{F}$ becomes:

$$\mathbf{F} = \frac{B_0^2}{\mu L}A^{(0)}\frac{dA^{(0)}}{dx}e^{-2y}\,\mathbf{i}_x, \tag{2.20}$$

where the asterisks have been omitted for convenience. It is noticeable that the electromagnetic forces are irrotational at the lowest order, since from (2.19) the $y$ component of $\nabla\Phi$ is greater than $\mathbf{F}$. More precisely,

$$|\mathbf{F}| = O(\epsilon)\left|\frac{\partial\Phi}{\partial y}\right|. \tag{2.21}$$

Using (2.16) and the computed distribution of the vector potential (cf. figure 2) in the expression (2.19) for $\mathbf{F}$, one may have a qualitative description of the Lorentz forces in the electromagnetic layer in both cases I and II. This is sketched in figure 4. In a quarter of a meridian plane $\mathbf{F}$ has two zeros in case I and three zeros in case II.

### 2.2. *The motion equations*

The electromagnetic force distribution being known, it is natural to consider the motion equations. The general equations of steady motion are

$$\rho(\mathbf{u}.\nabla)\,\mathbf{u} + \nabla(p+\Phi) = \mathbf{F} + \rho\nu\nabla^2\mathbf{u} + \rho\mathbf{g}, \tag{2.22a}$$

$$\nabla.\mathbf{u} = 0, \tag{2.22b}$$

where $\mathbf{u}$ is the velocity field, $p$ is the pressure, and $\mathbf{g}$ is the acceleration due to gravity. In (2.22$a$) the electromagnetic forces have been split using the decomposition (2.18).

First, let us examine qualitatively the temperature effects and compare the buoyancy forces to the Lorentz forces. The equation of state of the fluid is assumed to be

$$\rho = \rho_0(1-\alpha(T-T_0)), \tag{2.23}$$

where $T$ denotes the temperature and $\alpha$ the coefficient of thermal expansion. Any temperature variation $\Delta T$ leads to a density variation $\Delta\rho$ such that

$$\Delta\rho = -\alpha\rho_0\,\Delta T. \tag{2.24}$$

Using the Boussinesq approximation the buoyancy force is $\Delta\rho\mathbf{g}$. Let us consider the ratio

$$|\mathbf{F}|/|\Delta\rho\mathbf{g}|. \tag{2.25}$$

(2.25) may be evaluated by using the expression (2.20) for $\mathbf{F}$, hence

$$|\mathbf{F}|/|\Delta\rho\mathbf{g}| \sim \frac{B_0^2}{\mu\rho_0 gL\alpha\Delta T}. \tag{2.26}$$

From (2.26) the importance of buoyancy forces depends strongly on the magnitude of the characteristic temperature differences in the pool. If we consider for example a practical case, e.g. a five ton aluminium furnace (see appendix B for further details) it is found that the order of magnitude of the typical temperature differences due only to electromagnetic stirring is

$$\Delta T = 3{\cdot}4\,.\,10^{-2}\ ^\circ\mathrm{C}. \tag{2.27}$$

Using the numerical values given in appendix B with $\alpha = 0{\cdot}5\,.\,10^{-4}\ ^\circ\mathrm{C}^{-1}$ we obtain an estimate of the ratio (2.26):

$$|\mathbf{F}|/|\Delta\rho\mathbf{g}| = 7\,.\,10^3 \gg 1. \tag{2.28}$$

The above estimate shows that, although Joule dissipation is important, buoyancy is probably a secondary effect in the dynamics of the stirring. Therefore, the investigation will be focused on the electromagnetic effects, and density gradients will be neglected.

Let us now derive a non-dimensional form of the equations (2.22). Setting

$$\mathbf{u}_* = \mathbf{u}/u_0, \quad \nabla_* = L\nabla, \quad \mathbf{B}_* = \mathbf{B}/B_0, \tag{2.29}$$

where $u_0$ is the Alfvén speed defined in (1.4), the system (2.22) may be rewritten in the following form:

$$\mathbf{u}.\nabla\mathbf{u} + \nabla P = \mathbf{F} + R^{-1}\nabla^2\mathbf{u}, \quad R = u_0 L/\nu, \tag{2.30}$$

$$\nabla.\mathbf{u} = 0, \tag{2.31}$$

where the asterisk has been omitted for convenience. $P$ denotes the total pressure. Physically, equation (2.30) expresses a balance between inertia, the Lorentz forces and viscosity.

In the high frequency limit, it must be pointed out that $\mathbf{F}$ contains implicitly another length scale, i.e. the skin depth $\delta$. The driving force is localized in a wall layer, and it is natural to assume that $\delta$ is the proper length scale of variation of the velocity field transverse to the wall in the penetration layer. This leads to important simplifications of (2.30) in the electromagnetic layer. Indeed, using the local co-ordinates $(x, y)$ defined in §2 and denoting by $(u, v)$ the dimensionless velocity components respectively along $\mathbf{i}_x$, $\mathbf{i}_y$, the continuity equation (2.31) becomes

$$\frac{\partial}{\partial x}(h_2 u) + \frac{\partial}{\partial y}(h_2 v) = 0, \tag{2.32}$$

$h_2$ being defined in appendix A. From (2.32) it is clear that if $\delta$ is the right length scale in the $y$ direction, i.e.

$$\partial/\partial y = O(L/\delta) \quad \text{and} \quad \partial/\partial x = O(1), \tag{2.33}$$

then

$$v = O(\delta/L)\, u. \tag{2.34}$$

Since from (2.19) the rotational part of the Lorentz forces has a single component along $\mathbf{i}_x$ at the lowest order, (2.33), (2.34) imply that the classical boundary layer approximations may be used in the layer. The Navier–Stokes equations (2.30) then reduce to a single projection along the $x$ axis. With these approximations, it is convenient to rescale $y$ and $v$ as follows:

$$x \to x, \quad y \to y/\epsilon, \quad u \to u, \quad v \to \epsilon v. \tag{2.35}$$

Combining (2.20), (2.30) and (2.35) the dimensionless equations of motion in the layer reduce to:

$$u\frac{\partial u}{\partial x} + v\frac{\partial u}{\partial y} + \frac{\partial P}{\partial x} = A^{(0)}\frac{dA^{(0)}}{dx}e^{-2y} + \frac{1}{R}\epsilon^{-2}\frac{\partial^2 u}{\partial y^2} + O(\epsilon, 1/R), \quad \frac{\partial P}{\partial y} = 0, \tag{2.36}$$

the continuity equation (2.32) being unchanged. The boundary conditions are

$$\left.\begin{aligned} &u = v = 0 \quad \text{on} \quad y = 0, \\ &u \to U(x) \quad \text{as} \quad y \to +\infty, \end{aligned}\right\} \tag{2.37}$$

where $U(x)$ denotes the slip velocity of the flow in the interior region at the wall. There appears in (2.36) a new parameter

$$R_\delta = Re^2 = 2R/R_\omega,$$

representing an effective interaction parameter of the flow. In the interior region the motion is governed by equations (2.30), (2.31) where we set $\mathbf{F} = 0$.

## 3. Case I. The infinite circular cylinder

The aim of this section is to investigate an idealized situation, i.e. the circular cylinder in a uniform transverse magnetic field. Because of the various symmetries of the problem, the domain may be restricted to a quarter of a cylinder. The general motion equations are (2.30), and the corresponding boundary conditions are:

$$\left.\begin{aligned} &\zeta = \psi = 0, \quad \theta = 0, \frac{\pi}{2}, \\ &\psi = \frac{\partial \psi}{\partial r} = 0, \quad r = 1, \end{aligned}\right\} \tag{3.1}$$

where $\zeta$ denotes the single vertical vorticity component of the flow, and $\psi$ is the corresponding stream function. Both an asymptotic theory in the high frequency limit and numerical computations have been carried out.

### 3.1. *The asymptotic theory*

When $\epsilon$ is small, a perturbation analysis may be used to study the motion. We assume that the domain may be split into various regions as follows: (i) the interior region referred to as I; (ii) the electromagnetic layer referred to as II; (iii) the viscous boundary layers referred to as III (if viscosity is small). Two cases are distinguished according to the value of the parameters $R_\delta$ and $\epsilon$.

(*a*) *Large viscosity limit.* The simplest case corresponding to a purely viscous motion has been studied by Sneyd (1971). Inertia is assumed to be negligible in the whole domain. In the interior region $\zeta$ satisfies

$$\nabla^2 \zeta = 0, \tag{3.2}$$

and the stream function $\psi$ of the flow is related to $\zeta$ by

$$\nabla^2 \psi = -\zeta. \tag{3.3}$$

In the electromagnetic layer the inertial terms are also neglected, and (2.36) reduces to

$$\frac{dP}{dx} = A^{(0)} \frac{dA^{(0)}}{dx} e^{-2y} + \frac{1}{R_\delta} \frac{\partial^2 u}{\partial y^2}. \tag{3.4}$$

The expression for $A^{(0)}$ for a circular cylinder is given by (2.16) with $\theta = x$. In (3.4) the pressure gradient is actually of order of $\epsilon^2$ with respect to the terms of the right hand side and is neglected in the asymptotic theory. This may be readily justified by considering the order of magnitude of the pressure in the interior region. The solutions

satisfying (3.2), (3.3), (3.4) and the boundary conditions (3.1), (2.37) have the following form:

$$\zeta = \tfrac{3}{2} R_\delta r^2 \sin 2\theta \quad (\text{here } \theta \equiv x), \tag{3.5a}$$

$$\psi = \frac{R_\delta}{8}(r^2 - r^4)\sin 2\theta, \tag{3.5b}$$

$$u = \frac{R_\delta}{4}(1 - e^{-2y})\sin 2x. \tag{3.5c}$$

The maximum velocity is obtained with $y = +\infty$ and $x = \frac{1}{4}\pi$ in (3.5*c*), namely

$$u(\tfrac{1}{4}\pi, \infty) = \tfrac{1}{4} R_\delta. \tag{3.6}$$

The streamline pattern consists of four eddies in each of the four quadrants in the circular cross-section of the cylinder. It must be observed that the Reynolds number $R_e$ of the flow in the interior region is

$$R_e = u_0 R_\delta a/\nu = R R_\delta = R^2 \epsilon^2, \tag{3.7}$$

$a$ being the radius of the cylinder. Thus, solution (3.7) is valid only when

$$R_e = R^2 \epsilon^2 \ll 1.$$

(*b*) *Small viscosity limit.* In the other asymptotic situation, the interior region is assumed to be inviscid. The flow pattern may be split into three main zones: the interior region I, the electromagnetic layer II and the wall viscous layer III of depth $\delta_v$. Various cases occur according to the value of the ratio $\delta_v/\delta$ which from (2.36) is defined by

$$\delta_v/\delta = O(uR_\delta)^{-\frac{1}{2}}, \tag{3.8}$$

where $u$ is a characteristic velocity of the pool (a similar procedure was carried out by Sneyd 1971). In the limit $\delta_v/\delta \gg 1$, equation (3.4) is still valid in the region II, and (3.6) yields the characteristic velocity of the problem. Then, from (3.6), (3.8) the expression of $\delta_v$ is

$$\delta_v/a = O(R\epsilon)^{-1}.$$

In the small viscosity limit, we require for consistency that $R\epsilon \gg 1$. The transition between the two flow régimes corresponding to $\delta_v/\delta \gtrless 1$ depends on the value of $R_\delta$. In the analysis given here, we shall not distinguish between the regions II and III.

Consider first the region I, and assume that the flow consists of a single vortex lying wholly in I. This assumption is both supported by the results of the transient problem (Sneyd 1971) and verified *a posteriori* by the numerical calculations. In I, the Lorentz forces are identically zero, and viscosity is negligible. For a streamline lying in I, Batchelor's (1956) theorem holds, and vorticity is constant, namely

$$\zeta = \zeta_0 \text{ (a constant)}. \tag{3.9}$$

In I, the motion is governed by the following equations and boundary conditions:

$$\left.\begin{aligned} &\nabla^2\psi = -\zeta_0, \\ &\psi = 0 \quad \text{on} \quad r = 1 \,\forall\, \theta \quad \text{and} \quad \theta = 0, \frac{\pi}{2} \,\forall\, r. \end{aligned}\right\} \tag{3.10}$$

The solution of (3.10) may be sought by expanding $\zeta_0$ and $\psi$ in Fourier series as follows:

$$\left.\begin{aligned}\zeta_0 &= \sum_{n=1}^{\infty} \zeta_n \sin 2n\theta, \\ \psi &= \sum_{n=1}^{\infty} \psi_n(r) \sin 2n\theta,\end{aligned}\right\} \tag{3.11}$$

where the Fourier coefficients $\zeta_n$ are defined by

$$\zeta_n = \frac{2\zeta_0}{n\pi}(1-\cos n\pi) = \left\{\begin{matrix} 0 & (n \text{ even}), \\ -4\zeta_0/n\pi & (n \text{ odd}).\end{matrix}\right\} \tag{3.12}$$

The solution of (3.10) is:

$$\psi = -\zeta_1 \frac{r^2}{4} \log r \sin 2\theta + \sum_{n=2}^{\infty} \frac{\zeta_n}{4(n^2-1)} (r^{2n} - r^2) \sin 2n\theta. \tag{3.13}$$

It must be observed that the modulus of $\psi$ is still undetermined. From (3.13) the tangential velocity component at the wall, i.e. $U(\theta)$ is:

$$U(\theta) = -\left(\frac{\partial \psi}{\partial r}\right)_{r=1} = \zeta_1 \frac{\sin 2\theta}{4} - \sum_{n=2}^{\infty} \frac{\zeta_n}{2(n+1)} \sin 2n\theta. \tag{3.14}$$

The expression for $U(\theta)$ is necessary to match the interior region with the electromagnetic layer. Furthermore, $U(\theta)$ yields the pressure gradient in (2.36). Indeed, (2.36), (2.37) yield

$$\frac{\partial P}{\partial x} = -U \frac{dU}{dx} \quad (\text{here } x \equiv \theta). \tag{3.15}$$

Regarding the electromagnetic layer, a first approach consists of looking for solutions of (2.36) in Fourier series as follows:

$$\psi = f_1(y) \sin 2x + f_2(y) \sin 4x + \ldots. \tag{3.16}$$

Inserting (3.16) into (2.36), and comparing terms, we obtain a system of simultaneous ordinary differential equations for the functions $f_1, f_2, \ldots$. Such a system is very complicated. Therefore, in order to have some clues to the complete solution, we have retained only the first two harmonics. The equations governing $f_1, f_2$ are then

$$f_1'^2 - f_1 f_1'' = U_1^2 + \frac{1}{R_\delta} f_2''', \quad 2f_2 f_1'' - f_2' f_1' - f_1 f_2'' = U_1 U_2 + e^{-2y} + \frac{1}{R_\delta} f_1'''. \tag{3.17}$$

The boundary conditions on $f_1, f_2$ are:

$$f_1 = f_1' = f_2 = f_2' = 0 \quad \text{on} \quad y = 0, \quad f_1' = U_1, f_2' = U_2 \quad \text{at} \quad y = +\infty, \tag{3.18}$$

where $U_1$, $U_2$ denote the Fourier coefficients of $U(x)$. The values of $U_1$, $U_2$ are given by (3.14). Actually, from (3.12), (3.14) $U_2$ is zero, and $U_1$ is still undetermined. The system (3.17), (3.18) has been solved numerically by using a Runge–Kutta type scheme and a shooting method from the origin ($y = 0$). The value of $U_1$ was found numerically as an eigenvalue of the system. The results are shown in figures 5, 9 where $f_1', f_2'$ are plotted versus $y$ and the value of $U_1$ is plotted versus $R_\delta$ (dashed line). We observe in figure 9 that there exist two flow régimes according to the value of $R_\delta$ which from (3.8) is involved in the transition $\delta_v/\delta \gtrless 1$. The first branch (e.g. $R_\delta \lesssim 1$)

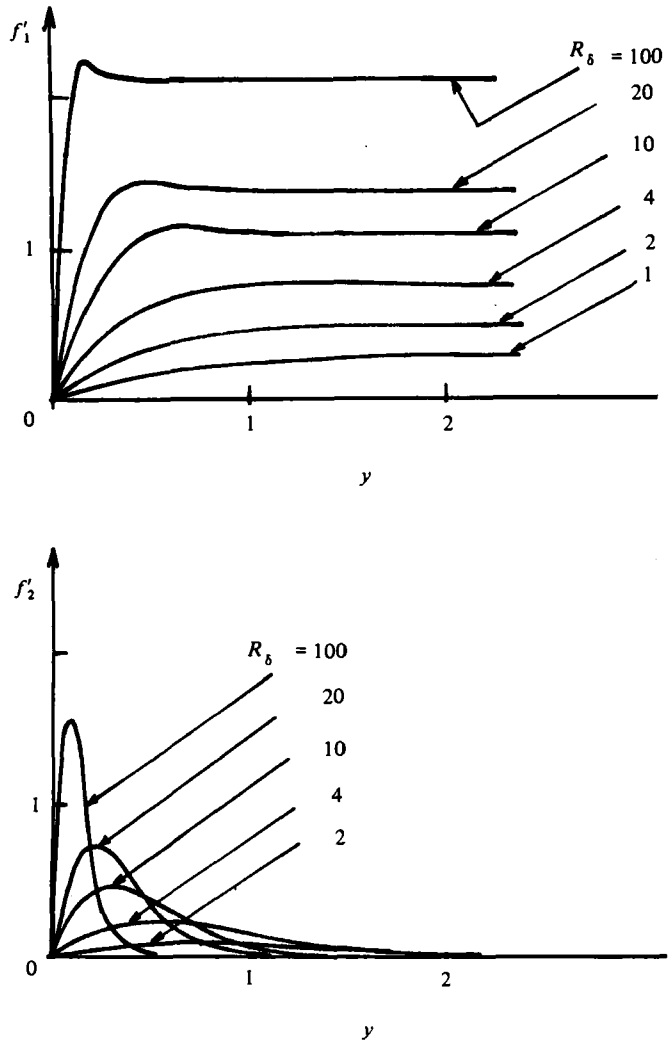


FIGURE 5. Theoretical tangential velocity profiles in the skin; $f_1'$, $f_2'$ corresponding to the two first harmonics are normalized by $u_0$.

probably corresponds to the continuation of the viscous solution where $U_1 = \frac{1}{4}R_\delta$ and $U_i = 0$, $i = 2, 3....$ As for the second one ($R_\delta > 1$) we have not been able to determine the exact asymptotic behaviour of $U_1$ for large $R_\delta$, but it is found numerically that

$$U_1 \propto R_\delta^\alpha \quad \text{with} \quad \alpha \simeq 0{\cdot}3.$$

From figure 5 it must be observed that, as $R_\delta$ increases, $f_2'$ behaves like a wall jet confined to a wall sublayer. Concerning the first harmonic, $f_1'$ is almost constant in the skin depth then changes rapidly near the wall. Such a behaviour is confirmed by an analytical solution of (3.17) with $R_\delta = \infty$. Indeed, the solution of (3.17) satisfying the following boundary conditions:

$$f_1(0) = 0, \quad f_1'(\infty) = U_1, \quad f_2(\infty) = \text{constant}, \quad f_2'(\infty) = 0,$$

is

$$f_1' = U_1, \quad f_2' = e^{-2\nu}/2U_1 y. \tag{3.19}$$

To interpret the above results, let us integrate (2.36) over $x$ from 0 to $\frac{1}{2}\pi$. Applying the boundary conditions (3.1) yields:

$$\int_0^{\frac{1}{2}\pi} v\frac{\partial u}{\partial y}dx = e^{-2\nu} + \frac{1}{R_\delta}\int_0^{\frac{1}{2}\pi}\frac{\partial^2 u}{\partial y^2}dx \quad \text{for any value of } y. \tag{3.20}$$

Moreover, let us assume that in the limit $R_\delta \gg 1$ there exists a wall viscous sublayer as the above solutions suggest. It is clear from considering the boundary conditions in the electromagnetic layer, that from (3.20) the $v$-component of the flow cannot be zero at the wall (unless $\partial u/\partial y$ becomes infinite). We are led to admit the existence of a flux, whose magnitude is at least $O(u_0\delta)$ across the sublayer. This is in agreement with the singular behaviour of $f_2'$ near $y = 0$ in (3.19). Such a flux is also consistent with the integral expression of Batchelor's theorem obtained by integrating (2.30) along a closed streamline $(C)$ (Sneyd 1971), namely

$$\oint_{(C)} \mathbf{F}.d\mathbf{l} + \frac{1}{R}\oint_{(C)} \nabla^2\mathbf{u}.d\mathbf{l} = 0. \tag{3.21}$$

According to (3.21) any streamline $(C)$ which crosses the penetration layer must also cross a viscous layer in the laminar steady-state approximation.

As for the interior flow, it must be observed that its magnitude is determined by the dynamics of the wall layers (II and III) via the parameter $U_1$. The fact that $U_1$ is an eigenvalue may be explained by the need of a sufficient pressure gradient in the layers II, III. The pressure gradient ensures that the boundary conditions on the tangential velocity component for $\theta = 0, \frac{1}{2}\pi$ are satisfied, i.e.

$$u(0, y) = u(\tfrac{1}{2}\pi, y) = 0.$$

We shall end this section with a short analysis of the singular zones along $\theta = 0, \frac{1}{2}\pi$. The solution in the interior region I cannot satisfy the boundary conditions (3.1) on $\zeta$. Therefore, there exist two free boundary layers in which the vorticity component varies from $\zeta_0$ to 0 along $\theta = 0, \frac{1}{2}\pi$. Let us consider for example the case $\theta = 0$ and adopt the new local variables $\hat{u}$, $\hat{v}$, $\zeta$ along the local co-ordinates $r$, $\eta$ such that:

$$\eta = O(\delta_v/a),$$

$\delta_v$ being the boundary layer thickness. Let $\hat{U}$ be the velocity outside the boundary layer. The expression of $\hat{U}$ is given by (3.13), namely

$$\hat{U}(r) = \frac{1}{r}\left(\frac{\partial\psi}{\partial\theta}\right)_{\theta=0}.$$

The boundary layer thickness is

$$\delta_v/a = O(\hat{U}u_0\, a/\nu)^{-\frac{1}{2}}.$$

The jump in velocity is of the order of $\delta_v\zeta_0 u_0/a$ ($u_0/a$ being the vorticity scale). The smallness of this variation of velocity across the boundary layer implies that the classical boundary layer equations may be linearized by setting (Batchelor 1967):

$$u = \hat{U}(r) + O(\delta_v/a).$$

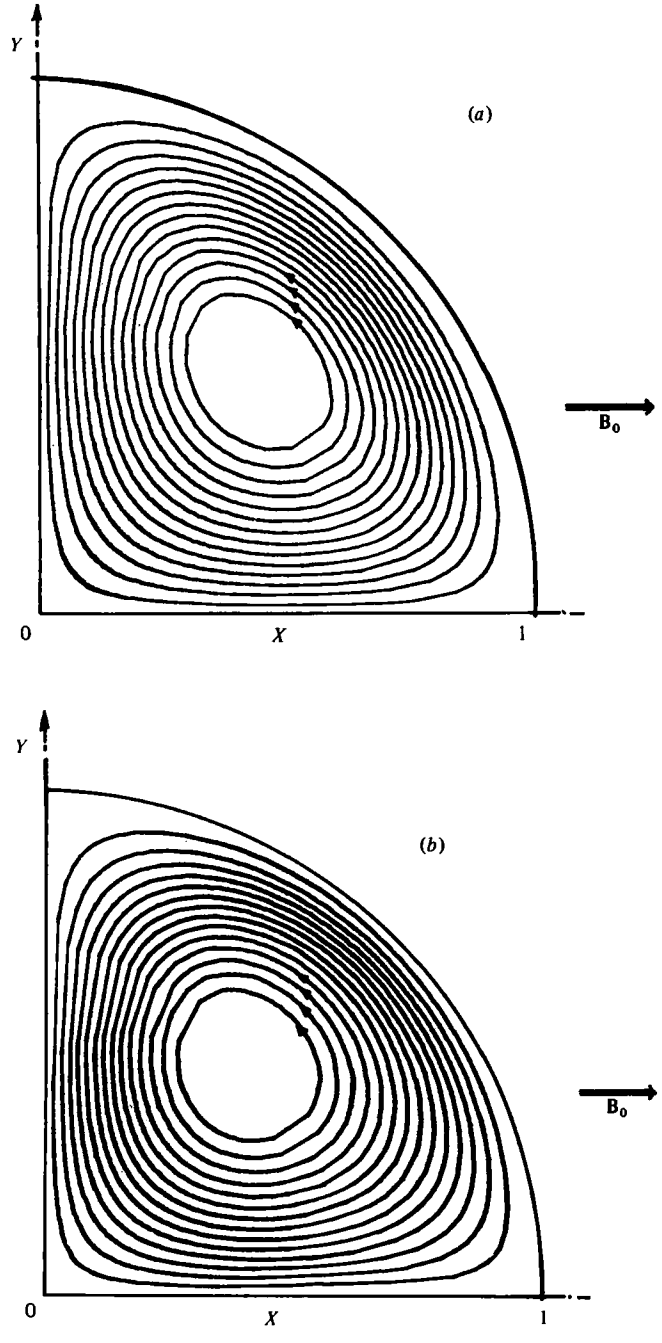


FIGURE 6. Streamline pattern in case I corresponding to the numerical solutions of Navier–Stokes equations for $R_\omega = 50$, and (*a*) $R = 50$, (*b*) $R = 500$. The domain is restricted to a quarter of a cylinder, and the values of $\psi$ can be deduced from the velocity profiles in figure 7.

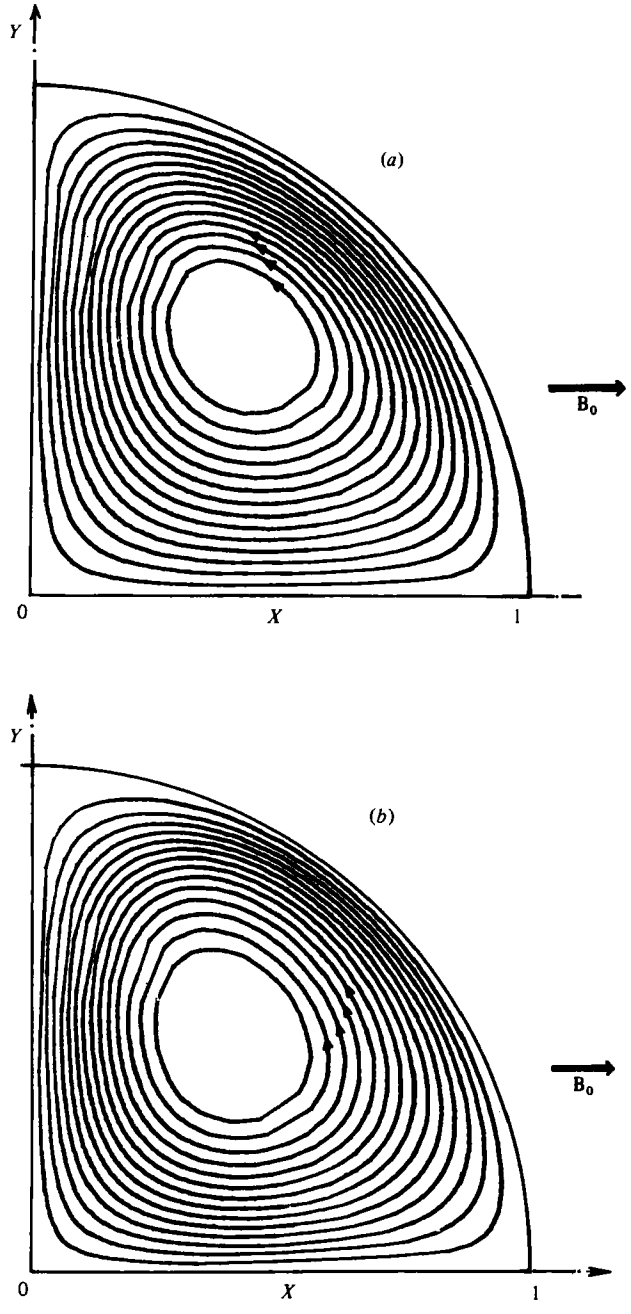


FIGURE 7. Streamline pattern in case I corresponding to the numerical solutions of Navier–Stokes equations for $R_\omega = 200$, and (*a*) $R = 200$, (*b*) $R = 2000$.

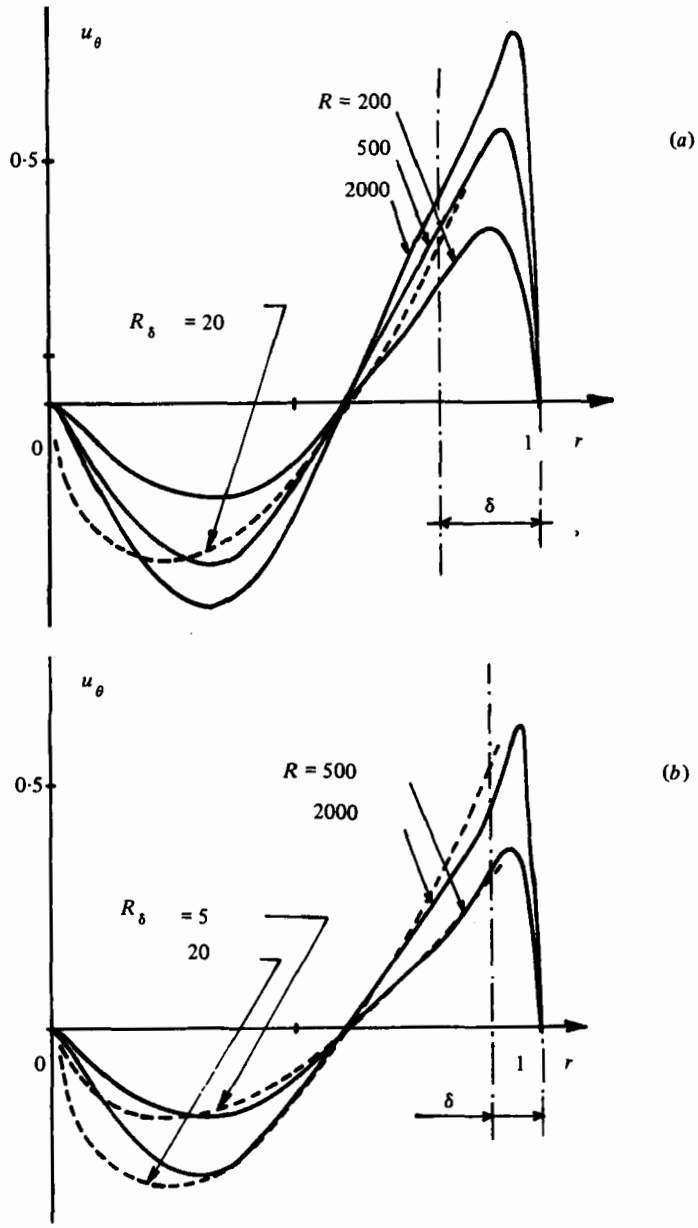


FIGURE 8. Tangential velocity profiles $u_\theta(r, \frac{1}{4}\pi)$ in case I: ——, computed profiles for (*a*) $R_\omega = 50$ and (*b*) $R_\omega = 200$. – – – –, profiles given by the asymptotic theory for $R_\delta = 5$ and 20.

The tendency for back flow to develop in the boundary layer is much weaker at a free surface than at a rigid wall (Batchelor 1967). Therefore, we shall not pay attention to those layers.

### 3.2. *The numerical solutions*

It is of interest to compare the asymptotic analysis with numerical work carried out in the same geometry. The Navier–Stokes equations (2.30), (2.31) have been solved numerically in a quarter of a circular cylinder in a transverse uniform magnetic field.

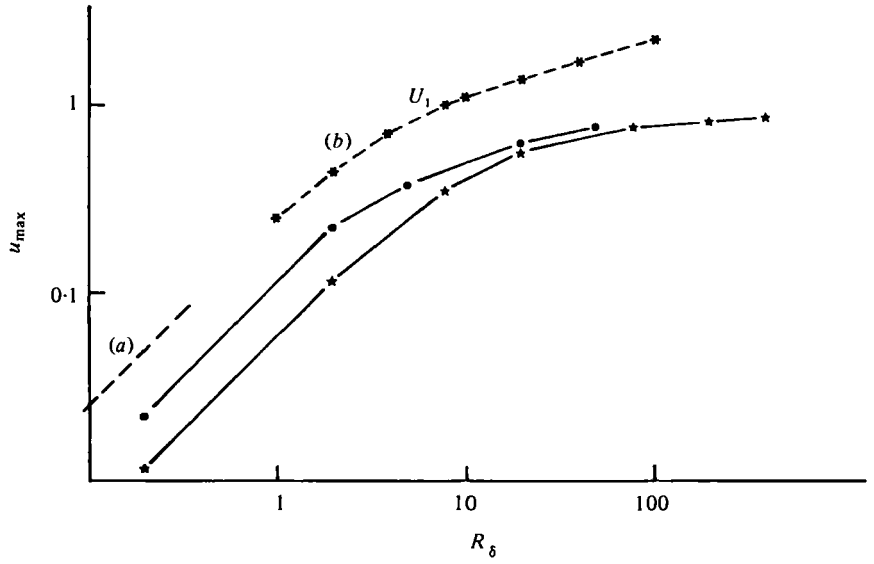


FIGURE 9. Maximum computed velocity $u_{max}$ in the pool in case I (solid lines) and first coefficient of Fourier expansion $U_1$ of the flow in the interior region (dashed line), given by the asymptotic theory; (*a*) is obtained from the viscous solution, and (*b*) corresponds to the case $R_\delta \gtrsim 1$; the velocities are normalized by $u_0$. ★, $R_\omega = 50$; ●, $R_\omega = 200$.

The asymptotic expression (2.20) of the Lorentz forces (valid for high frequencies) has been used in the computations. The steady state solutions are obtained by computing the single vorticity component $\zeta$ and the streamfunction $\psi$ (for a complete discussion see Khaletzky 1976). The boundary conditions on $\psi$ and $\zeta$ are given by (3.1). A finite difference scheme coupled with an integration of the equations in the mesh is used. The number of points is $28 \times 29$. The convective terms are discretized by using upstream differences. This method ensures the stability of the numerical scheme, but on the other hand it introduces a numerical diffusion which limits the validity of the solutions for large Reynolds numbers. The investigation may be split into two parts: (*a*) the analysis of the flow pattern, and (*b*) the analysis of the flow régime, i.e. the variation of the typical velocity with respect to the interaction parameter $R_\delta$.

(*a*) *Flow pattern.* The results are shown in figures 6, 7, 8. The flow pattern consists of one vortex in a quarter of a cylinder. In accordance with the initial assumptions of §3.1, two main regions may be distinguished: (i) the interior region; (ii) the wall boundary layers. In the interior region, the flow configuration and the shape of the tangential velocity profile are insensitive to the value of $R$ when $R \gg 1$ (figures 6, 7, 8). The flow consists of closed streamlines in the central region. The corresponding analytical velocity profiles obtained for $R_\delta = 5$ and 20 are plotted in figures 7(*a*, *b*) (dashed lines). The agreement between the computed and analytical curves is fairly good except near the origin. This is possibly an effect of the side boundary layers. As for the wall layers, one observes an increase of the tangential velocity near the wall as $R_\delta$ increases (figure 8).

(*b*) *Flow régime.* In figure 9 the maximum computed value of the velocity in the pool, $u_{max}$, has been plotted versus $R_\delta$ on logarithmic scales. For $R_\delta \lesssim 1$, the curves are almost parallel to the one-power law in accordance with (3.4). However, for

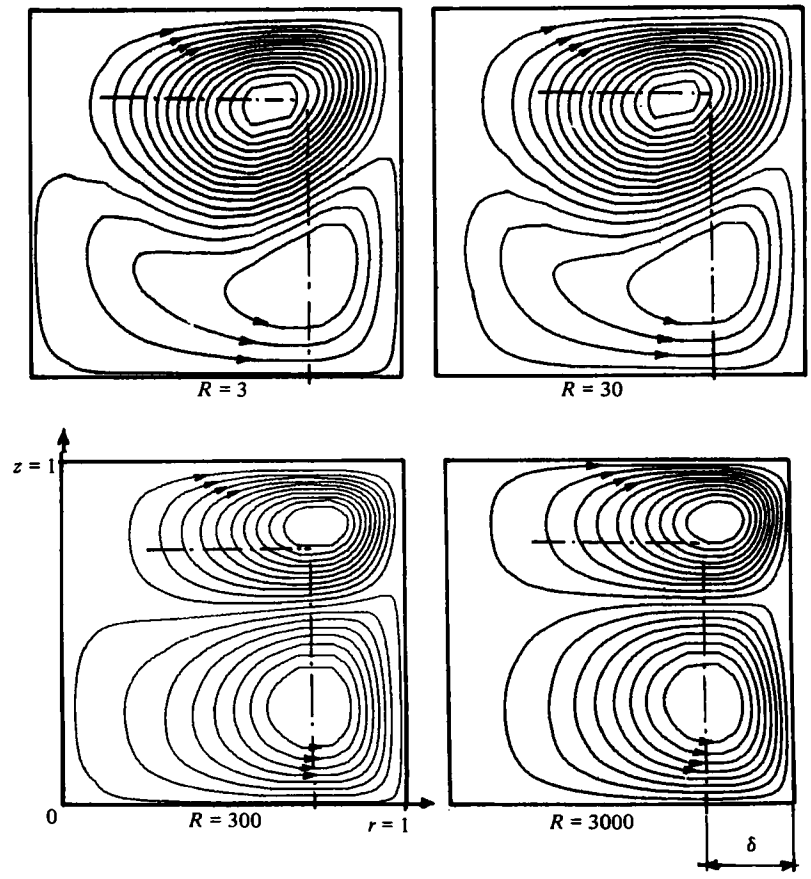


FIGURE 10. Streamline pattern in a half meridian plane of a truncated circular cylinder (case II) corresponding to the numerical solutions of Navier–Stokes equations for $R_\omega = 30$; the values of $\psi$ can be deduced from the velocity profiles in figure 12.

$R_\delta > 1$, we observe a change of the slope of the various curves in an analogous way to the asymptotic curve $U_1(R_\delta)$. We have not been able to determine the asymptotic behaviour of $u_{\max}(R_\delta)$, since for large $R_\delta$ it is likely that numerical diffusion overcomes viscous diffusion. However, it is noteworthy that, when $R_\delta \sim 1$, $u_0$ (cf. (1.4)) is a good estimate of the velocity in the pool (cf. figure 9).

## 4. Case II. The truncated circular cylinder

Only numerical work has been undertaken in this case. An asymptotic theory might be developed in principle as in §3.1. However, the geometry, and particularly the presence of the corners, introduce some difficulties, especially when using a local frame. The numerical procedure is similar to that of §3.2. The electromagnetic force distribution has been computed (cf. §2.1) neglecting the electric currents induced by the motion, and then introduced in the motion equations. Owing to the symmetry of the force distribution, the domain may be restricted to a half meridian plane. The number of grid points is $19 \times 19$. The boundary conditions are analogous to (3.1).

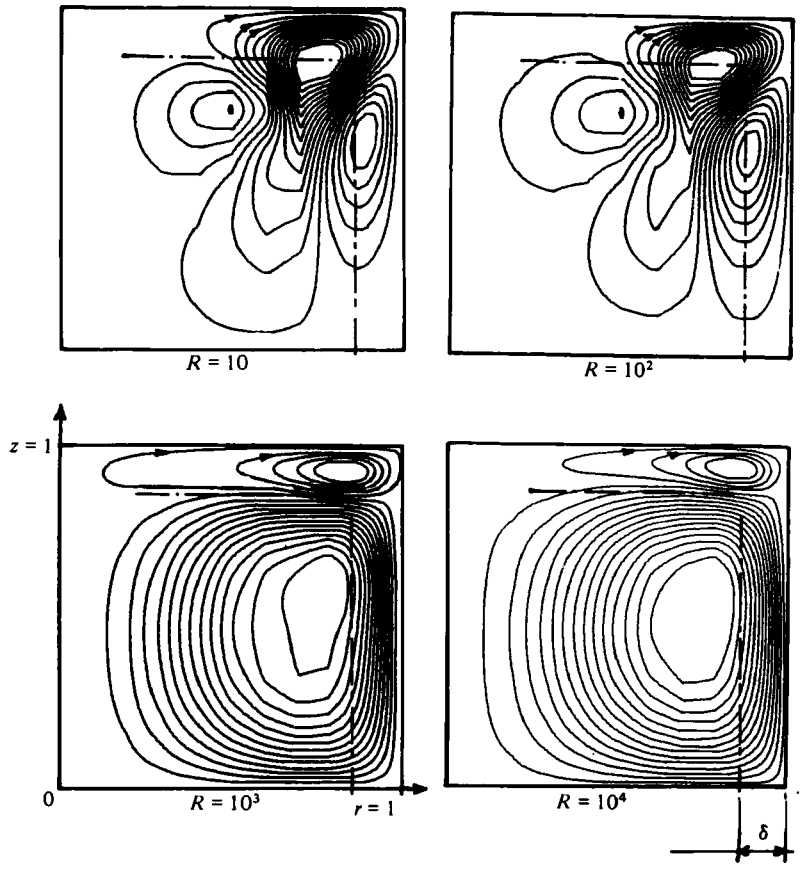


FIGURE 11. Streamline pattern in a half meridian plane of a truncated circular cylinder (case II); $R_\omega = 100$.

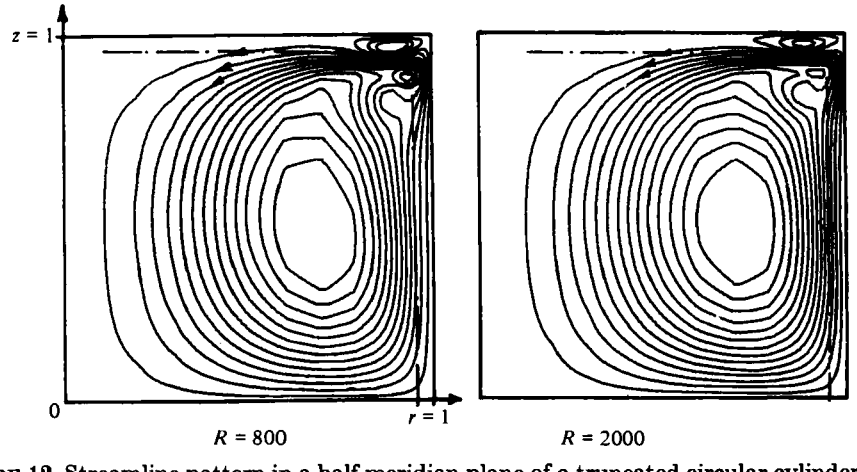


FIGURE 12. Streamline pattern in a half meridian plane of a truncated circular cylinder (case II); $R_\omega = 800$.

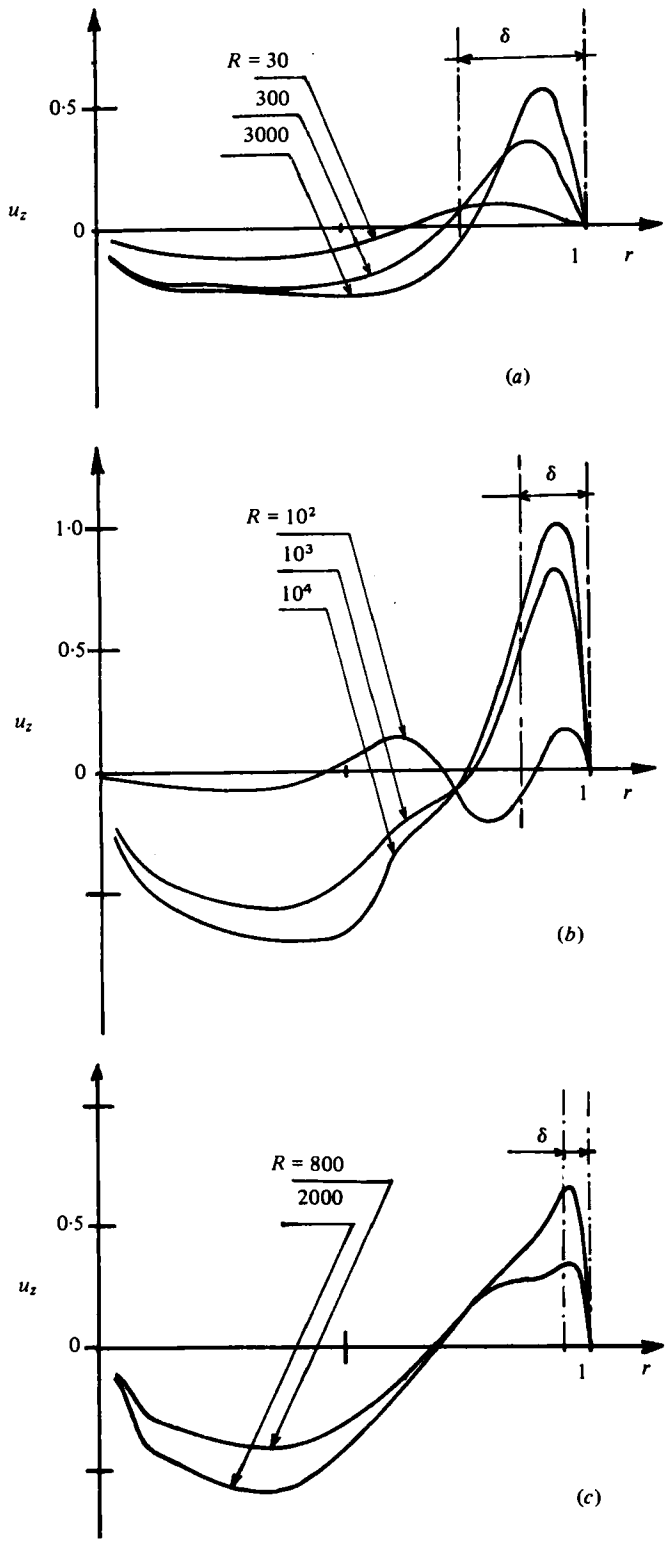


FIGURE 13. Computed vertical velocity profiles $u_z$ $(r, z = 0{\cdot}7)$ in case II, (*a*) $R_\omega = 30$, (*b*) $R_\omega = 100$, (*c*) $R_\omega = 800$; the velocities are normalized by $u_0$.

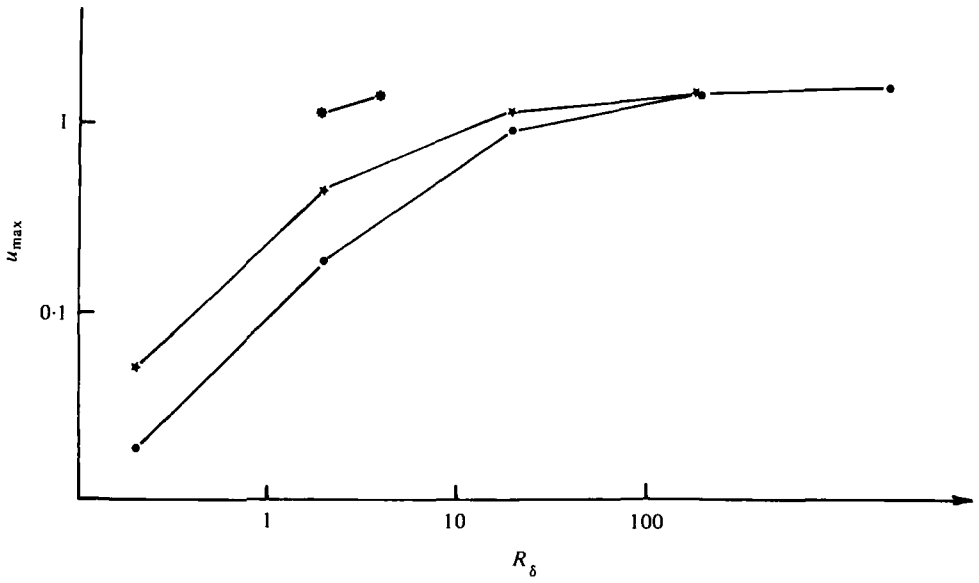


FIGURE 14. Maximum computed velocity $u_{max}$ in the pool (case II); the velocities are normalized by $u_0$. ●, $R_\omega = 30$; ★, $R_\omega = 100$; *, $R_\omega = 800$.

Again, the investigation may be split into the analysis of the flow configuration and the flow régime.

(*a*) *Flow pattern.* The flow configurations consist of two or three vortices in a half meridian plane according to the values of $R_\omega$ and $R$. More precisely, it must be noticed that for a fixed $R_\omega$ (figures 10, 11, 12) the magnetic field strength which is represented by $R$, no longer has any influence on the motion pattern whenever $R_\delta$ is greater than unity or $Re$ large enough. This is also shown in figure 13 where the vertical velocity component is plotted versus the radius of the pool for $R_\omega = 30$, 100, 800 and various values of $R$. In that figure, for $R_\delta > 1$ and for fixed $R_\omega$, the shape of the velocity profiles is similar in the interior region in all cases. Moreover, this figure shows (especially figure 13*c*) an increase of the flow in the electromagnetic layer. In the high-frequency limit and with $R_\delta \gtrsim 1$ that result may be explained by the existence of two distinct regions (cf. §3.1): (i) an inviscid central region where

$$\zeta/r = \text{a constant}, \tag{4.1}$$

according to Batchelor's theorem; and (ii) an electromagnetic layer which may contain a wall viscous sublayer. In the interior region the flow pattern is fixed by (4.1) up to a constant and does not change when $R_\delta \gtrsim 1$. The existence of a second vortex (cf. figures 11, 12), whose size is roughly proportional to the skin depth, may be a consequence of the special distribution of the vector potential along the wall (see figure 2). Indeed, the vector potential reaches a maximum value near the corner, and according to (2.20) the driving forces are positive on the side wall and negative on the upper one (in the local co-ordinates) as it is shown in figure 4.

(*b*) *Flow régime.* Viscous effects are also involved in the determination of the proper velocity scale of the various flow régimes. The maximum computed value of the

velocity $u_{\max}$ has been plotted versus $R_\delta$ in figure 14. We also observe two flow régimes according to $R_\delta \gtrless 1$. For $R_\delta \lesssim 1$, the slopes of the curves are almost unity in accordance with what should be expected from the continuation of the viscous solution in the electromagnetic layer. However, for $R_\delta > 1$ the slopes of the various curves are less than unity. For very large values of $R_\delta$, $u_{\max}$ tends to a constant. In that case, the asymptotic behaviour of $u_{\max}$ is not significant because of numerical diffusion.

## 5. Discussion

In summary, the basic parameters of the problem are the frequency, the magnetic field strength and the viscosity which are involved via the non-dimensional numbers $R_\omega$, $R$ and $R_\delta$ respectively. Dealing with the motion, we have demonstrated that when $R\epsilon$ is large, the field strength no longer has an influence on the flow pattern but only on the magnitude of the velocity field. In this case, a transition régime is found according to $R_\delta \gtrless 1$. The proper velocity scale is either $u_0 R_\delta$ when $R_\delta \lesssim 1$ or $u_0 R_\delta^{0.3}$ when $R_\delta \gtrsim 1$.

The above treated is based on the assumption of laminar flow. However the Reynolds numbers are generally large, and the flow in most practical cases will be turbulent. Nevertheless, various experiments (Cremer 1979) indicate that in this case there exist well-organized mean (i.e. time-averaged) structures. Though one has to be cautious in interpreting these experiments because of thermal convection which cannot be rigorously dissociated from electromagnetic stirring, this mean motion is probably driven by the electromagnetic forces. Therefore, we claim that most of the results of this paper may be applied to the mean constituent of the flow, at least in a heuristic way. Of course, molecular viscosity must then be replaced by an effective viscosity (eddy viscosity). For very large Reynolds numbers, the viscous dissipation comes mainly from turbulent small-scale fluctuations, and, in analogy with turbulent boundary layers on rough walls, there might exist a third flow régime where the mean velocities are independent of the viscosity.

The author is indebted to Prof. R. Moreau for having suggested this problem and for helpful comments, and to Prof. H. K. Moffatt for suggestions which led to improvements in the paper.

## Appendix A. Definition of the local co-ordinates $(x, y)$ associated with a given geodesic curve

Consider a given curve (e.g. the boundary of the pool, cf. figure 1) and its equations in a parametric representation. Any point on the curve is represented by its cylindrical co-ordinates $(r_0(x), z_0(x))$ $((X_0, Y_0)$ in the two-dimensional case) which are both function of the parameter $x$, namely

$$r_0(x) = R(x), \quad z_0(x) = S(x), \tag{A 1}$$

where $x$ denotes the curvilinear abscissa defined from B taken as the origin (figure 1). Let us consider any point $M$ whose local co-ordinates are $(x, \theta, y)$ $y$ being the distance of $M$ from the wall $((x, y, z)$ in two-dimensions). $(x, \theta, y)$ is a system of orthogonal

curvilinear co-ordinates, and if $dl$ is the distance between two neighbouring points we have:

$$dl^2 = h_1^2 dx^2 + h_2^2 d\theta^2 + h_3^2 dy^2, \tag{A 2}$$

where in the usual notation $h_1$, $h_2$, $h_3$ are defined by

(i) in the axisymmetric geometry:

$$h_1 = 1 + yR''(x)/S'(x), \quad h_2 = r(x), \quad h_3 = 1, \tag{A 3}$$

(ii) in the two-dimensional case:

$$h_1 = 1 + yR''(x)/S'(x), \quad h_2 = h_3 = 1. \tag{A 4}$$

Thus, the differential operator $\mathscr{L}$, defined by

$$\mathscr{L}(\cdot) \equiv \nabla \times \nabla \times ((\cdot)\,\mathbf{i}_\theta),$$

takes the following form

$$\mathscr{L}(\cdot) \equiv -\left\{\frac{1}{h_1}\frac{\partial}{\partial x}\left[\frac{1}{h_1 h_2}\frac{\partial}{\partial x}(h_2(\cdot))\right] + \frac{1}{h_1}\frac{\partial}{\partial y}\left[\frac{h_1}{h_2}\frac{\partial}{\partial y}(h_2(\cdot))\right]\right\}. \tag{A 5}$$

An interesting particular case occurs when

$$\partial/\partial x = O(1/L), \quad \partial/\partial y = O(1/\delta), \tag{A 6}$$

where $\delta \ll L$, $L$ being a typical length of the boundary. Indeed, we may set

$$h_1 = 1 + O(\delta/L), \quad h_2 = R(x) + O(\delta/L). \tag{A 7}$$

The expressions (A 7) are valid except when the curvature of the boundary becomes large, namely

$$R''(x)/S'(x) = O(L/\delta). \tag{A 8}$$

## Appendix B. Estimates of the temperature gradients in a crucible

In this appendix we shall estimate the characteristic temperature difference $\Delta T$ in a standard practical case: a five-ton aluminium furnace. The characteristic parameters of the furnace are:

radius, $L = 0{\cdot}6$ m;

height, $H = 0{\cdot}8$ m;

typical magnetic field, $B_0 = 2{\cdot}10^{-2}\,T$;

frequency, $f = 50$ Hz.

The physical properties of aluminium at $T = 700$ °C are:

electrical conductivity, $\sigma = 5{\cdot}10^6$ mho m$^{-1}$;

specific heat, $C_p = 10^3$ J kg$^{-1}$ °C$^{-1}$;

thermal conductivity, $\lambda = 10^2$ J/ms$^{-1}$ °C$^{-1}$;

density, $\rho_0 = 2{\cdot}37.10^3$ kg m$^{-3}$.

The energy equation which governs the temperature distribution $T$ is:

$$\underset{①}{\frac{\partial T}{\partial t}} + \underset{②}{\mathbf{u}.\nabla T} = \underset{③}{\chi \nabla^2 T + \langle \mathbf{j}^2 \rangle / \rho_0 C_p \sigma}, \tag{B 1}$$

where $\mathbf{j}$ denotes the induced electrical current density, $\langle \mathbf{j}^2 \rangle / \sigma$ is the mean Joule dissipation in the bath per unit volume (averaged over one period), $\mathbf{u}$ is the velocity field and

$$\chi = \lambda / \rho_0 C_p = 0{\cdot}42 . 10^{-4} \text{ MKS}.$$

Using the above numerical values, let us estimate the orders of magnitude of each term of (B 1) in order to estimate $\Delta T$. Let us adopt $u_0$ as the proper velocity scale, so that $\Delta T$ will be a measure of the homogeneity of the pool due to the electromagnetic stirring. The orders of magnitude are:

$$① = u_0 \Delta T / L, \tag{B 2}$$

$$② = \chi \Delta T / \delta^2, \tag{B 3}$$

$$③ = B_0^2 \omega / 2\mu\rho_0 C_p = u_0^2 \omega / 2C_p. \tag{B 4}$$

In (B 4) we have used (2.3), (2.11). Indeed, since the magnetic field component $B_x$ parallel to the wall is such that

$$B_x = O(B_0),$$

the order of magnitude of the electrical current density is

$$\mathbf{j} = O(B_0 / \mu\delta).$$

The role of diffusion with respect to convection by the velocity field is measured by the following ratio

$$②/① = \chi L / u_0 \delta^2 = R_\omega / 2P_e, \tag{B 5}$$

where

$$P_e = u_0 L / \chi.$$

Using the numerical values yields

$$R_\omega = 710, \quad u_0 = 0{\cdot}36 \text{ m/s}, \quad \delta/L = 0{\cdot}053, \quad ②/① = 0{\cdot}065.$$

The above result indicates that convection by the motion dominates over thermal molecular diffusion. Thus, the proper temperature difference may be obtained by equating the convection term ① to the Joule heat source ③, namely

$$u_0 \Delta T / L = u_0^2 \omega / 2C_p,$$

so that

$$\Delta T = u_0 \omega L / 2C_p = 3{\cdot}4 . 10^{-2} \text{ °C}. \tag{B 6}$$

Though the above estimate (B 6) is formal, it gives a clue as to the good homogeneity of the bath due to the stirring (including turbulent effects). Note that these conclusions are confirmed by recent experiments performed in a mercury pool by Cremer (1979) who found that the maximum temperature difference in the bath was indeed at most 1 °C.

## REFERENCES


Batchelor, G. K. 1956 *J. Fluid Mech.* **1**, 177.

Batchelor, G. K. 1967 *An Introduction to Fluid Dynamics*. Cambridge University Press.

Cremer, P. 1979 Thèse de Docteur-Ingénieur, Université de Grenoble.

Khaletzky, D. 1976 Thèse de 3ème cycle, Université de Grenoble.

Moffatt, H. K. 1965 *J. Fluid Mech.* **22**, 521.

MOFFATT, H. K. 1978 Some problems in the magnetohydrodynamics of liquid metals. *Z. angew. Math. Mech.* **58**, 65.

MOFFATT, H. K. 1980 *Proc. 2nd Bat-Sheva Seminar in M.H.D. Flows and Turbulence* (1978) (ed. H. Branover). Wiley.

MOREAU, R. 1980 *Proc. 2nd Bat-Sheva Seminar on M.H.D. Flows and Turbulence* (1978) (ed. H. Branover). Wiley.

SNEYD, A. 1971 *J. Fluid Mech.* **49**, 817.

SNEYD, A. 1979 *J. Fluid Mech.* **92**, 35.

SZEKELY, J. & NAKANISHI, K. 1975 *Metallurgical Trans.* B **6**, 245.

TARAPORE, E. D. & EVANS, J. W. 1976 *Metallurgical Trans.* B **8**, 179.

TIR, L. L. 1976 *Magnit. Gidrod.* **2**, 100.